NeuroImage 191 (2019) 176–185

Contents lists available at ScienceDirect

NeuroImage

journal homepage: www.elsevier.com/locate/neuroimage

Imaging beta amyloid aggregation and iron accumulation in Alzheimer's disease using quantitative susceptibility mapping MRI

Nan-Jie Gong [a,*], Russell Dibb [b], Marjolein Bulk [c], Louise van der Weerd [c], Chunlei Liu [d,e,**]

[a] *Shanghai Research Center for Brain Science and Brain-Inspired Intelligence, Shanghai, China*
[b] *Center for In Vivo Microscopy, Duke University School of Medicine, Durham, NC, USA*
[c] *Department of Radiology & Human Genetics, Leiden University Medical Center, the Netherlands*
[d] *Electrical Engineering and Computer Sciences, University of California, Berkeley, CA, USA*
[e] *Helen Wills Neuroscience Institute, University of California, Berkeley, CA, USA*

ARTICLE INFO

Keywords:
Magnetic resonance imaging
Alzheimer's disease
Beta amyloid
Iron
Magnetic susceptibility

ABSTRACT

Beta amyloid is a protein fragment snipped from the amyloid precursor protein (APP). Aggregation of these peptides into amyloid plaques is one of the hallmarks of Alzheimer's disease. MR imaging of beta amyloid plaques has been attempted using various techniques, notably with T2* contrast. The non-invasive detectability of beta amyloid plaques in MR images has so far been largely attributed to focal iron deposition accompanying the plaques. It is believed that the T2* shortening effects of paramagnetic iron are the primary source of contrast between plaques and surrounding tissue. Amyloid plaque itself has been reported to induce no magnetic susceptibility effect. We hypothesized that aggregations of beta amyloid would increase electron density and induce notable changes in local susceptibility value, large enough to generate contrast relative to surrounding normal tissues that can be visualized by quantitative susceptibility mapping (QSM) MR imaging. To test this hypothesis, we first demonstrated in a phantom that beta amyloid is diamagnetic and can generate strong contrast on susceptibility maps. We then conducted experiments on a transgenic mouse model of Alzheimer's disease that is known to mimic the formation of human beta amyloid but without neurofibrillary tangles or neuronal death. Over a period of 18 months, we showed that QSM can be used to longitudinally monitor beta amyloid accumulation and accompanied iron deposition *in vivo*. Individual beta amyloid plaque can also be visualized *ex vivo* in high resolution susceptibility maps. Moreover, the measured negative susceptibility map and positive susceptibility map could provide histology-like image contrast for identifying deposition of beta amyloid plaques and iron. Finally, we demonstrated that the diamagnetic susceptibility of beta amyloid can also be observed in brain specimens of AD patients. The ability to assess beta amyloid aggregation non-invasively with QSM MR imaging may aid the diagnosis of Alzheimer's disease.

1. Introduction

Alzheimer's disease (AD) is a progressive neurodegenerative disease and the most prevalent type of dementia in the elderly. The most common early symptoms of AD are difficulty learning and poor memory. Due to the lack of a reliable biomarker sensitive to early pathologic changes, a probable diagnosis of the disease can only be made during advanced stages by employing clinical-based criteria (Albert et al., 2011) with assistance from morphological biomarkers such as hippocampal atrophy. It is believed that microscopic changes take place long before gross morphological changes (Gong et al., 2017) and the onset of clinical symptoms such as memory loss (Rose et al., 2008). Development of a reliable biomarker sensitive to abnormalities at the microscopic and pathological level for early diagnosis and monitoring progression of the disease is therefore urgently needed (Dubois et al., 2014).

Although the cause of the disease is not fully understood, clinical and neuropathological studies have hypothesized that the formation of beta amyloid (Aβ) plaques and tau neurofibrillary tangles is central to pathogenesis of AD. Aβ peptides including Aβ40 and Aβ42 are found to be the major components of senile plaques commonly present in AD (Sisodia and Price, 1995). Many studies suggest that these peptides can form toxic oligomers and fibrils under physiological conditions and can rapidly

---

* Corresponding author. Building 12, No. 100, Haike Road, Pudong District, Shanghai, 201210, China.
** Corresponding author. 505 Cory Hall, Berkeley, CA, 94720-1770, USA.
E-mail addresses: nanjie.gong@gmail.com (N.-J. Gong), chunlei.liu@berkeley.edu (C. Liu).

https://doi.org/10.1016/j.neuroimage.2019.02.019
Received 8 October 2018; Received in revised form 16 January 2019; Accepted 6 February 2019

aggregate (Benilova et al., 2012). In the amyloid hypothesis, plaque buildup has been linked to accelerated oxidative stress that will result in neuronal loss (Hardy and Higgins, 1992). Accordingly, detection of abnormal beta amyloid aggregation becomes crucial for identifying AD related pathological changes. *In vivo* pathology of Aβ has also been advocated now as part of the AD diagnostic criteria (Dubois et al., 2014).

To benefit the development of diagnostics and therapeutics at preclinical stages, radiotracers that highlight deposits of beta amyloid in PET scan such as ^{11}C-based Pittsburgh compound B (Klunk et al., 2004) and ^{18}F-based compounds (e.g. Florbetapir) (Lister-James et al., 2011) have been developed to image beta amyloid *in vivo*. However, the major drawbacks of PET—namely ionizing radiation, low resolution, and the current high cost —limit its application in clinical routine settings for early screening. Alternatively, non-invasive and radiation-free imaging of beta amyloid plaque using MRI with higher spatial resolution would be a major step forward towards early diagnosis and prognosis of the disease. In addition to probing associated microstructural degeneration using diffusion techniques (Gong et al., 2013, 2017), MR methods with enhanced contrast through injecting exogenous agents such as gadolinium (Gd) and monocrystaline iron oxide nanoparticles have been investigated for indirectly detecting beta amyloid plaques (Poduslo et al., 2002). Non-invasive methods utilizing endogenous contrast based on transverse proton relaxation rate (R2*) have also been assessed for detecting beta amyloid masses and especially accompanied focal iron accumulation (Jack et al., 2005; Meadowcroft et al., 2009).

The non-invasive detectability of beta amyloid plaques on MR images has so far been largely attributed to focal iron deposition accompanying the plaques (Borthakur et al., 2006; Chamberlain et al., 2009; Dhenain et al., 2002b; El Tannir El Tayara et al., 2006; El Tayara Nel et al., 2007; Falangola et al., 2005; Jack et al., 2004; Vanhoutte et al., 2005; Wengenack et al., 2011). Amyloid plaque has been reported to induce no magnetic susceptibility effect (Dhenain et al., 2002a). It is believed that the T2* shortening effects of paramagnetic iron are the primary source of contrast between plaques and surrounding tissue (Jack et al., 2004). However, the iron content associated with plaques varies greatly between the thalamus and hippocampus, as well as between transgenic mouse and human (Leskovjan et al., 2009; Vanhoutte et al., 2005; Wengenack et al., 2011). A study on APP/PS1 transgenic mice reported that plaques are equally observable as human plaques even though they contain significantly less iron load (Meadowcroft et al., 2009). Iron deposits have also been observed in tau neurofibrillary tangles. The relationship between amyloid plaque density and iron concentration in AD is thus not straightforward or immediately clear. To explain the source of contrast, other studies have proposed potential alternative mechanisms such as water exchange between tissue and amyloid protein (Jack et al., 2004) or reduced cerebral blood flow (Helpern et al., 2004).

It is well known that proteins in general (there are exceptions) tend to be diamagnetic due to their high concentrations of paired electrons (Babaei et al., 2017). Therefore, we hypothesized that aggregations of purely beta amyloid would increase electron density and induce notable changes in local susceptibility large enough to generate contrast relative to surrounding normal tissues. On the other hand, iron in the brain is paramagnetic. Deposits consisting of both beta amyloid and iron would produce opposing effects on bulk tissue magnetic susceptibility that can be imaged with quantitative susceptibility mapping (QSM), a recently developed MRI method for quantifying local magnetic susceptibility value from MR phase images (Acosta-Cabronero et al., 2013; Deistung et al., 2017; Gong et al., 2018; Haacke et al., 2015; Langkammer et al., 2012; Liu et al., 2015a, 2015b; Schweser et al., 2016; Wang and Liu, 2015).

To test this hypothesis, we first examined the polarity of magnetic susceptibility of synthetic beta amyloid in phantom experiments. We then conducted QSM experiments on a transgenic mouse model of amyloidosis that is known to mimic the formation of human Aβ, but does not present with neurofibrillary tangles or neuronal death (Cook et al., 2014; Davis et al., 2004). We studied the mice longitudinally over a period of 18 months to assess beta amyloid accumulation and accompanied iron deposition *in vivo*. We also examined if individual beta amyloid plaques can be visualized *ex vivo* in high resolution susceptibility maps. The measured negative susceptibility map and positive susceptibility map were then compared with histological straining of beta amyloid and iron for validation. Finally, we compared QSM images of postmortem brain material of AD patient with histological stainings.

2. Methods and materials

2.1. Beta amyloid phantom

To examine the susceptibility properties of beta amyloid as well as tau protein, a cylindrical phantom with five straws that were 5.5 mm in diameter and 50 mm in length was used. The five straws contained gadolinium (0.5 mmol/ml, gadoteridol, ProHance®), beta amyloid buffer only, beta amyloid with buffer solution, tau protein buffer only, and tau protein with buffer solution. The beta amyloid (Aβ42, human) solution and its buffer were made using the SensoLyte® Thioflavin T Beta-Amyloid Aggregation Kit from Anaspec (Fremont, CA). In the solution, 0.5 mg beta amyloid protein was dissolved in 2 ml assay buffer, which was an optimized fibrillation buffer. Aβ42 peptide is pretreated to ensure it is in a monomeric state. The tau protein and its buffer were obtained from rPeptide (Bogart, GA). In the solution, 50 μL tau isoforms was mixed with assay buffer to generate a 2 ml solution.

The straws were placed in a large container filled with saline solution. The thin wall of the straws (about 100 μm) ensured that the susceptibility effects created by the straws were negligible. The five straws were separated by two plastic disks with five holes designed to align the straws in the container. The plastic disks were placed at the top and bottom of the phantom.

2.2. Beta amyloid transgenic mouse models

Four pairs of transgenic mice with abnormal beta amyloid aggregation (Tg-SwDI) and wild type were acquired from the Jackson Laboratory. These transgenic mice (Aβ mice) exhibit increasing expression of human amyloid beta precursor protein and insoluble beta amyloid 40 and 42 peptides initially in the subiculum, hippocampus and cortex (Davis et al., 2004). At six months of age, the diffuse plaque-like deposits increase in number and spread to the olfactory bulb and thalamic region. Beta amyloid deposits have been detected throughout the forebrain by 12 months of age in this mouse model. Notably, this model does not produce neurofibrillary tangles nor any significant neuronal death, thus making it ideally suitable for testing the magnetic susceptibility properties of aggregated beta amyloid in the brain.

2.3. MR imaging protocols

Phantom imaging was performed on a 7.0T scanner with 220 mm Magnex horizontal bore magnet and Agilent Direct Drive console. The phantom was positioned in the coil so that the long axes of the straws were parallel to the B0 field. A multi-echo, 3D gradient echo sequence was used with the following parameters: flip angle = 30°; $TE_1/\Delta TE/TE_6 = 4.91/3.19/20.85$ms; TR = 150ms; field of view = 54 × 54 × 54 mm^3; NEX = 1; spatial resolution = 210 μm isotropic; scan time was about 41 min (Fig. 1a).

Mouse models were imaged seven times longitudinally from 70 days to 538 days after birth. *In vivo* longitudinal imaging was performed using a CryoProbe on a 20 cm bore 7T scanner (Bruker BioSpec 70/20USR, Billerica, MA) with an Avance III system. The mouse was positioned in the coil so that the anterior-posterior axis of the brain was parallel to the B0 field. A respiratory gated multi-echo, 3D gradient echo sequence was performed with the following parameters: flip angle = 35°; $TE_1/\Delta TE/TE_{10} = 3.72/5.52/53.36$ ms; TR = 250ms; field of view = 19.2 × 14.4 × 9.6 mm^3; spatial resolution = 87.3 μm isotropic; NEX = 1. The total acquisition time

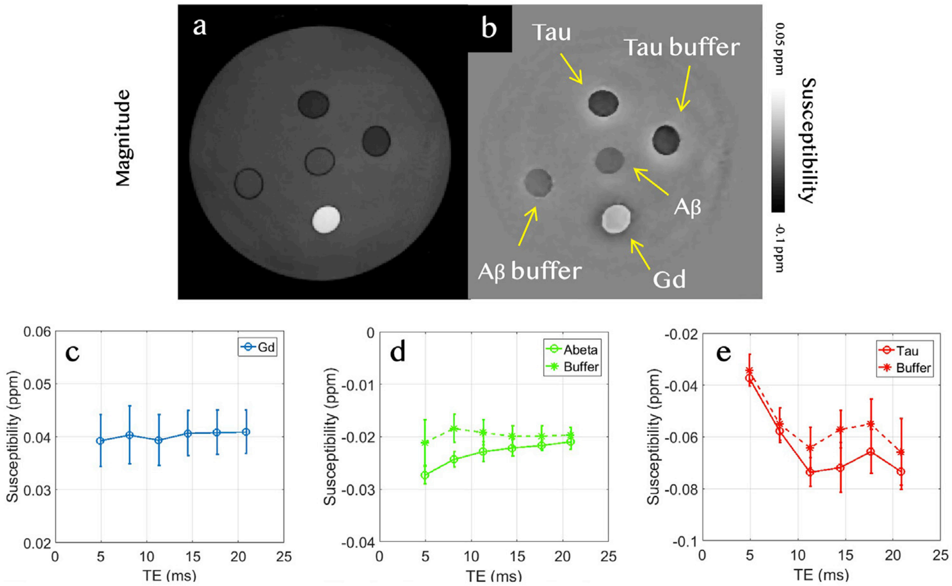

Fig. 1. T2*-weighted magnitude at TE of 4.91 ms (a) and susceptibility map (weighted-average value from all echoes, b) of the phantom. Beta amyloid solution manifested lower susceptibility values relative to its buffer (d), exhibiting a diamagnetic property. Susceptibility values of tau protein were also comparatively lower than its buffer (e).

was about 90 min. *In vivo* animal studies were performed using approved protocols under the Duke IACUC.

After the final *in vivo* imaging, mice were perfused with a peristaltic pump with a mixture of warm (37 °C) 0.9% saline and ProHance (10:1, v:v) (Bracco Diagnostics, Princeton, NJ), then followed by a mixture of 10% buffered formalin and ProHance (10:1, v:v) (Johnson et al., 2002). After perfusion fixation, the heads of the mice were stored in 20% buffered formalin overnight before imaging experiments in the following day. Imaging was performed on a scanner with 9.4 T (400 MHz) 8.9-cm vertical bore Oxford magnet controlled by an Agilent VnmrJ 4.0 console. A multi-echo, 3D gradient echo sequence was performed with the following parameters: flip angle = 20°; $TE_1/TE_2/TE_3 = 4.8/14.0/23.2$ms; TR = 120ms; matrix = 1000 × 550 × 500; spatial resolution = 20 µm isotropic; NEX = 1; scan time was about 9 h.

2.4. Image processing for quantitative susceptibility mapping

Image phase was first unwrapped using a Laplacian-based phase unwrapping algorithm (Li et al., 2011). The magnitude image was used to extract the brain tissue masks. Background phase was removed using a spherical mean value filtering, with an initial kernel width of 30 voxels and the kernel width decreasing toward the tissue boundary (Li et al., 2011; Schweser et al., 2011; Wu et al., 2012). The local susceptibility value was derived using an iLSQR algorithm (Li et al., 2011, 2015). Weighted-average susceptibility values from all echo times were calculated as the final susceptibility map. All algorithms were implemented in Matlab (Mathworks, Natick, MA, USA) using STI Suite (https://www.eecs.berkeley.edu/~chunlei.liu/software.html). In the calculation process, whole brain averaged susceptibility value was used as an internal reference.

2.5. Quantitative analysis of susceptibility maps

For analysis of longitudinal *in vivo* data of mice, one wild type mouse brain at the last scanning time point was selected as the template. The other brain image volumes were registered to this template by using an affine registration tool with degrees of freedom of 12. Then for each mouse, a general linear model included in FSL (FMRIB, Oxford, UK) was used to examine the correlation between QSM and age in a voxel-wise fashion with 5000 permutations. Family-wise error was corrected with significance set at p value of 0.05.

For comparison between *in vivo* data and *ex vivo* data, the *in vivo* longitudinal maps of each mouse were registered to their corresponding *ex vivo* map by using an affine registration tool with degrees of freedom of 12. Then a similar voxel-wise analysis using a general linear model was performed.

Susceptibility values of the hippocampus and caudate putamen at the age of 80 days and 216 days were compared between Aβ-depositing mice and wild type mice using Mann-Whitney *U* test. The CSF susceptibility value was also measured to provide an internal reference. Statistical analysis was performed using SPSS software with significance set at the level of $p < 0.05$. Results are described in figures as mean ± standard deviation.

2.6. Histological staining for beta amyloid and iron

After MR imaging, mouse brain hemispheres were fixed in 4% formaldehyde for 24hr before sucrose cryoprotection (10%, 20%, 30%). Sagittal slices of the mouse brain were sliced at a thickness of 25 µm on a cryostat. Sections were collected directly onto slide and were stored at −20° until staining. Tissue sections were then co-stained for iron and beta amyloid using diaminobenzide (DAB) enhanced Prussian blue reaction (Meadowcroft et al., 2015) followed by an aqueous thioflavin-S stain (Meadowcroft et al., 2015). The staining was performed at Histology Research Core Facility in University of North Carolina, Chapel Hill.

2.7. Human brain specimen

To investigate if magnetic susceptibility contrast induced by amyloid can be observed in AD patients, postmortem brain samples of the frontal lobe were obtained from 1 control brain and 2 AD patients. Tissues were fixed in 4% phosphate-buffered formalin. From each sample, one tissue block of approximately 20 × 15 × 15 mm was resected and washed in phosphate-buffered saline for 24 h to remove formalin. Each tissue block was submerged in Fomblin oil and scanned on a 7T horizonal bore Bruker MRI system (Bruker Biospin, Ettlingen, Germany) with a multiple gradient echo sequence: FOV = 24 × 14 × 12 mm, matrix = 240 × 140 x 120, 4 echoes, TE1 = 12.5 ms, echo spacing = 10.7 ms, TR = 75 ms, flip angle = 25°. Following MRI, the tissue blocks were embedded in paraffin. A 20-μm thick section was used for histochemical iron staining using a modified Meguro protocol (van Duijn et al., 2013). Two 8-μm thick sections were used for staining of beta amyloid (6F/3D anti-human Aβ antibody, DakoCytomation, Glostrup, Denmark) and paired helical filament tau (AT8 antibody, Innogenetics, Ghent, Belgium) respectively, as described (Bulk et al., 2018).

3. Results

3.1. Susceptibility of beta amyloid phantom

The susceptibility of gadolinium is almost independent of TE with a small fluctuation around an average value of 0.039 ppm (Fig. 1c). The mean standard deviation was 0.004 ppm. The susceptibility of beta amyloid solution has a mean value of −0.024 ppm with a mean standard deviation of 0.002 ppm. The susceptibility of amyloid buffer has a mean value of −0.019 ppm with a mean standard deviation of 0.003 ppm (Fig. 1d). The averaged susceptibility difference between beta amyloid solution and buffer was −0.005 ppm. The susceptibility value of tau solution decreased with the increase of TE. The value changed from −0.037 ppm to −0.071 ppm with a mean standard deviation of 0.005 ppm. However, most of the TE-dependence of the susceptibility is due to the tau buffer solution, which has a similar pattern of decrease with increase of TE. The value changed form −0.036 ppm to −0.063 ppm, with a mean standard deviation of 0.007 ppm (Fig. 1e). At later echoes, the tau solution is significantly more diamagnetic than the buffer solution.

3.2. Age-related susceptibility changes in Aβ mice

After registering *in vivo* data of individual mice to a native common template, quantitative susceptibility maps for the different time points were imported into a general linear model to test for correlations with age. Significant positive correlations with age were found in widespread areas in Aβ mice. The common regions exhibiting positive correlations included the caudate putamen, hypothalamus, substantia innominata, as well as somatosensory areas of the cerebral cortex (Fig. 2).

Negative correlations with age were observed mainly in the forebrain cortex, midbrain, cerebellar cortex and thalamus as well as white matter fiber tracts such as the corpus callosum, fornix and anterior commissure (Fig. 2).

No significant correlation with age was observed in the wild type mice.

3.3. Group differences in susceptibility between Aβ mice and wild type mice

Regions of interest of the hippocampus and caudate putamen were manually outlined in reference to the Allen Mouse Brain Atlas using ImageJ (https://imagej.nih.gov/ij/). In Aβ-overexpressing mice, the mean susceptibility values of the hippocampus and caudate putamen on both hemispheres were all higher than in wild type mice at both 80 days and 216 days of age. At the age of 216 days, significant difference was observed in the left hippocampus ($-1.54 \pm 0.33 \times 10^{-3}$ ppm for Aβ mice, $-2.67 \pm 0.32 \times 10^{-3}$ ppm for wild type mice, $p = 0.002$) (Table 1). Note that while the left hippocampus was less diamagnetic in the Aβ mice than in the WT at both 80 days and 216 days, it became more diamagnetic at 216 days (- $1.54 \pm 0.33 \times 10^{-3}$ ppm) than 80 days (- $1.45 \pm 1.32 \times 10^{-3}$ ppm) in the Aβ mice. Susceptibility values of CSF were around 26×10^{-3} ppm for both groups at the age of 80 days and 216 days (Table 1).

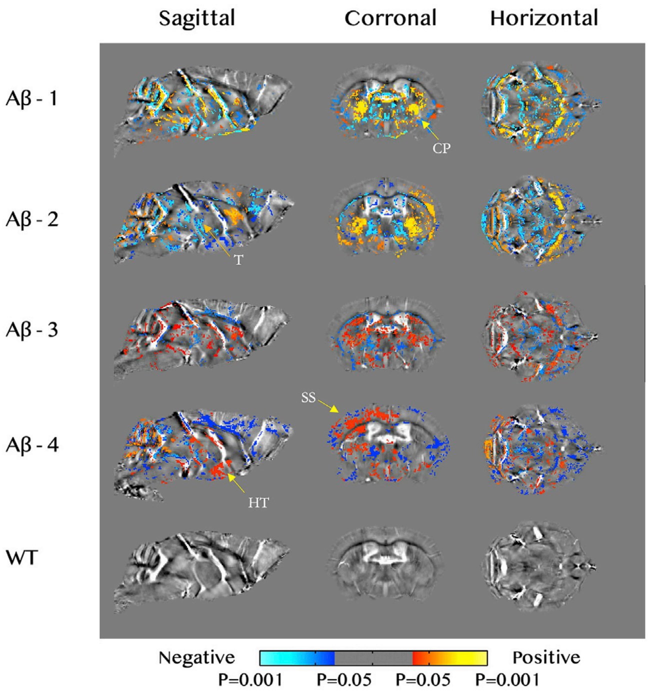

Fig. 2. Age-related increases of susceptibility value were commonly observed in the caudate putamen (CP), hypothalamus (HT), as well as somatosensory (SS) areas of the cerebral cortex of Aβ mice, as pointed by yellow arrows. Negative correlations with age were observed mainly in the forebrain cortex, midbrain, cerebellar cortex and thalamus (T) as well as white matter fiber tracts such as the corpus callosum, fornix and anterior commissure, as pointed by blue arrows. No significant correlation was observed in the wild type.

3.4. Identification of individual beta amyloid plaques on high resolution ex vivo susceptibility maps

Several salient focal spots of negative susceptibility values can be visually identified in high resolution *ex vivo* susceptibility maps of an Aβ mouse (Fig. 3). These relatively diamagnetic spots are likely beta amyloid plaques. Fig. 3 shows that these suspected plaques are located near CA1 of the hippocampus and dorsal auditory cortex (A), barrel field and forelimb region of primary somatosensory cortex, and cingulate cortex (B), barrel field of primary somatosensory cortex (C), forelimb region and jaw region of primary somatosensory cortex (D, E, F), CA1 in the hippocampus (G, H) and medical entorhinal cortex (I).

3.5. Comparison between in vivo longitudinal correlation and ex vivo high-resolution susceptibility map

As shown in Fig. 4, in an example of Aβ mouse brain, a cluster of voxels within the primary somatosensory cortex can be identified that exhibited a significant and negative correlation between susceptibility value and age.

At the same location on the *ex vivo* high-resolution susceptibility map, we found several focal spots exhibiting strong diamagnetism. The diamagnetic spots were located in the primary somatosensory cortex with a nearly perfect spatial correspondence to the position of the cluster that exhibited negative correlation with age on *in vivo* correlation maps.

3.6. Diamagnetic susceptibility map and paramagnetic susceptibility map

Anatomical structures of opposing magnetic properties were highlighted separately based on the *ex vivo* scans in diamagnetic susceptibility maps (thresholded negative susceptibility maps) and paramagnetic susceptibility maps (thresholded positive susceptibility maps) (Fig. 5). In the diamagnetic susceptibility maps, white matter fibers including the internal capsule, external capsule, corpus collosum, brachium of the superior colliculus, dorsal hippocampal commissure, glomerular layer of the olfactory bulb and arbor vitae in the cerebellum were highlighted (C

Table 1
In vivo susceptibility measurements ($\times 10^{-3}$ ppm) in Aβ and wile type mice at 80 days and 216 days after birth.

	80 days			216 days		
	Aβ	Wild Type	P	Aβ	Wild Type	P
left hippocampus	- 1.45 ± 1.32	- 2.67 ± 1.40	0.225	- 1.54 ± 0.33	- 2.67 ± 0.32	0.002**
right hippocampus	- 1.68 ± 0.44	- 2.41 ± 1.45	0.332	- 1.50 ± 1.24	- 2.51 ± 0.57	0.065
left caudate putamen	- 0.48 ± 1.71	- 1.61 ± 0.63	0.282	0.24 ± 1.88	- 1.60 ± 0.55	0.144
right caudate putamen	- 0.90 ± 0.78	- 1.57 ± 1.61	0.448	- 0.76 ± 1.85	- 1.57 ± 1.50	0.504
CSF	26.06 ± 1.56	26.55 ± 2.58	0.734	26.73 ± 1.50	26.71 ± 1.18	0.979

Values are in mean ± standard deviation.

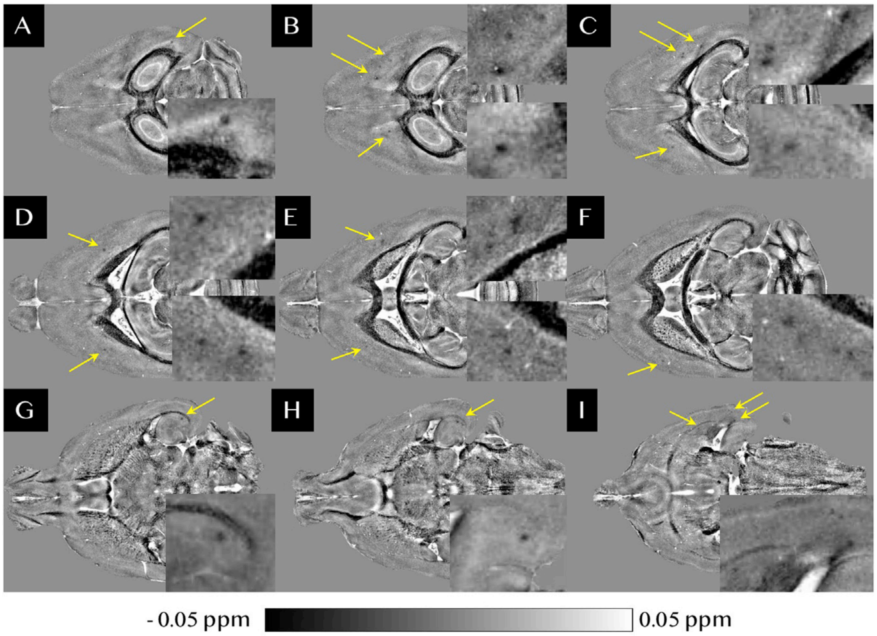

Fig. 3. On *ex vivo* susceptibility map, focal spots exhibiting salient diamagnetic susceptibility can be observed near CA1 of the hippocampus and dorsal auditory cortex (A), barrel field and forelimb region of primary somatosensory cortex, and cingulate cortex (B), barrel field of primary somatosensory cortex (C), forelimb region and jaw region of primary somatosensory cortex (D, E, F), CA1 in the hippocampus (G, H) and medical entorhinal cortex (I).

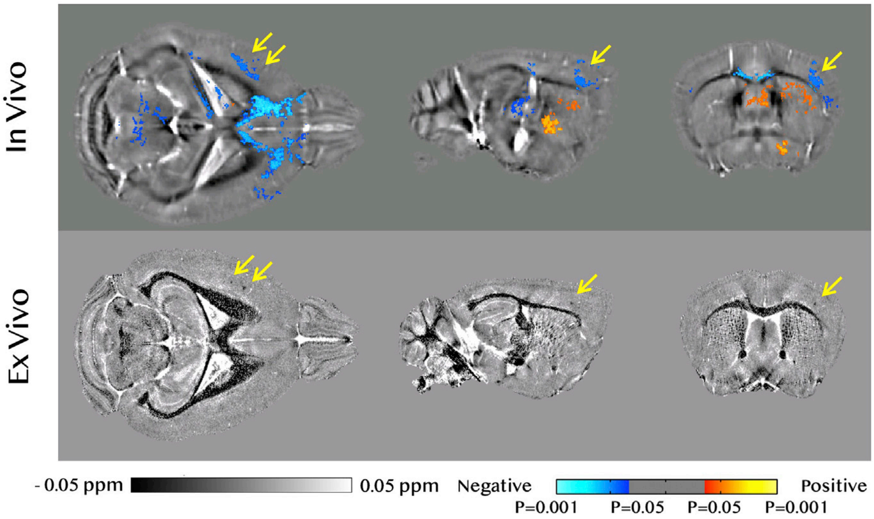

Fig. 4. Comparison between *in vivo* and *ex vivo* susceptibility maps. A cluster within the primary somatosensory cortex exhibiting a significant negative correlation (arrows) between susceptibility value and age *in vivo* had a near perfect spatial correspondence with several focal spots exhibiting strong diamagnetism (arrows) *ex vivo*, in a Aβ mouse.

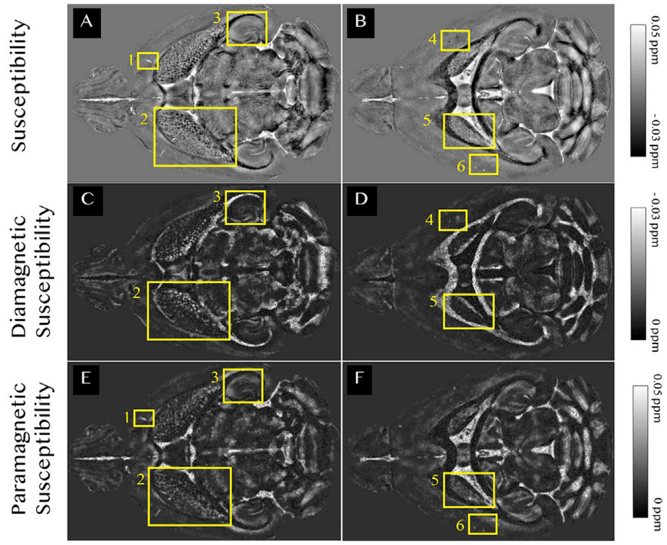

Fig. 5. In region (1) and region (6), vessels with residual Gd were highlighted in the paramagnetic susceptibility map (E & F). In region (2), the nigrostriatal pathway with myelinated axons was highlighted in diamagnetic susceptibility map (C), while iron deposition in the caudate putamen were highlighted in paramagnetic susceptibility map (E). In region (3), the dorsal hippocampal commissure with myelinated axons was highlighted in diamagnetic susceptibility map (C), while iron deposition in the stratum oriens of hippocampus were highlighted in paramagnetic susceptibility map (E). In region (4), possible beta amyloid plaques were highlighted in diamagnetic susceptibility map (D). In region (5), the internal capsule was highlighted in diamagnetic susceptibility map (D), while iron deposition in the caudate putamen were highlighted in paramagnetic susceptibility map (F). Note that the display scale in diamagnetic susceptibility maps (C & D) is reversed with bright intensity representing negative susceptibility values.

& D). In the paramagnetic susceptibility maps, gray matter areas in the cerebral cortex, hippocampus, thalamus, cerebellum as well as residual Gd in vessels and ventricles were highlighted (E & F) (Fig. 5).

Specifically, in region (1) and region (6), vessels with residual Gd were highlighted in the paramagnetic susceptibility map (E & F). In region (2), the nigrostriatal pathway with myelinated axons was highlighted in the diamagnetic susceptibility map (C), while ferritin content and possible iron deposition in the caudate putamen were highlighted in the paramagnetic susceptibility map (E). In region (3), the dorsal hippocampal commissure with myelinated axons was highlighted in the diamagnetic susceptibility map (C), while ferritin content and possible iron deposition in the stratum oriens of hippocampus were highlighted in the paramagnetic susceptibility map (E). In region (4), possible beta amyloid plaques were highlighted in the diamagnetic susceptibility map (D). In region (5), the internal capsule was highlighted in the diamagnetic susceptibility map (D), while ferritin content and possible iron deposition in the caudate putamen were highlighted in the paramagnetic susceptibility map (F).

3.7. *Comparison between magnetic susceptibility maps and histological stains*

The diamagnetic susceptibility map provided clear contrast for myelinated white matter tracts and putative beta amyloid plaques vs. surrounding tissues (Fig. 6). Near the alveus and splenium of corpus callosum surrounding hippocampus (a), diamagnetic components corresponded well with beta amyloid plaques in thioflavin-S stain. Similar strong spatial correspondences between focal diamagnetic components captured on the diamagnetic susceptibility map and beta amyloid plaques on thioflavin-S stain were also noted in the thalamus near brachium

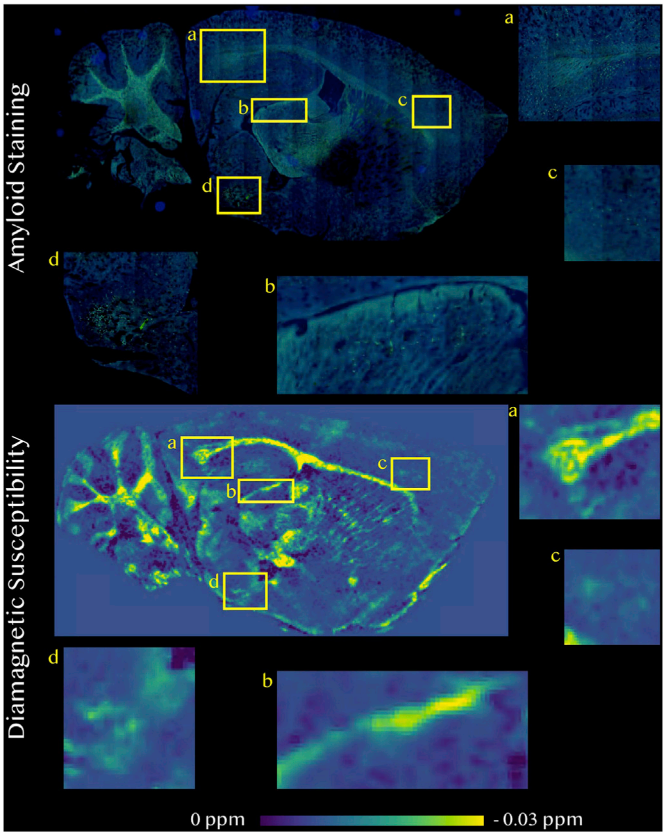

Fig. 6. Near the alveus and splenium of corpus callosum surrounding hippocampus (a), high diamagnetic susceptibility region corresponded spatially with beta amyloid plaques in thioflavin-S stain. Similar strong spatial correspondences between focal diamagnetic components and beta amyloid plaques on thioflavin-S stain were also noted in the thalamus near brachium of the superior colliculus (b), forebrain cortex near genu of the corpus callosum (c), and cortical amygdalar area (d).

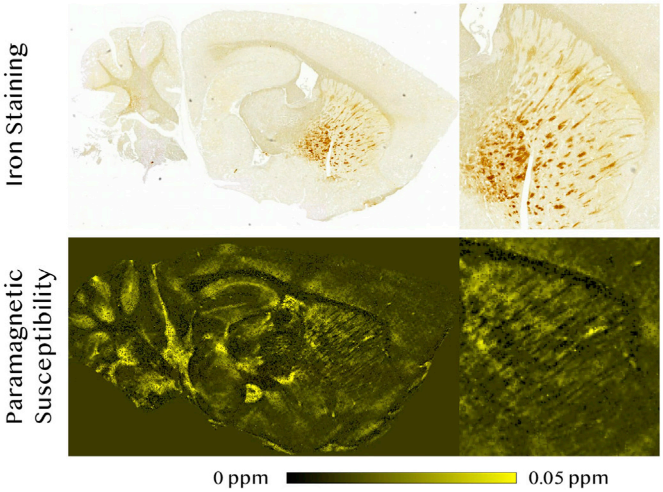

Fig. 7. In DAB enhanced Prussian blue stain for iron, notable iron deposition can be visualized throughout the caudate putamen area, correspondingly structures exhibiting strong paramagnetism were also identifiable on paramagnetic susceptibility map.

of the superior colliculus (b), forebrain cortex near genu of the corpus callosum (c), and cortical amygdalar area (d).

The paramagnetic susceptibility map of the same slice (Fig. 7) provided matching contrast for ferritin content and iron deposition. In the Prussian blue stain for ferric iron, notable iron deposition can be visualized throughout the caudate putamen. Corresponding structures exhibiting strong paramagnetism were also identifiable on the paramagnetic susceptibility map. In the pyramidal layer and stratum oriens of the hippocampus, components with strong paramagnetism can be observed while similar strong iron deposition was not observed on Prussian blue stain, suggesting variations in the sensitivity of the stain.

3.8. Human brain specimen

The control subject has a very low staining intensity of both beta amyloid and tau (Fig. 8A). Iron staining clearly highlights the boundaries between gray and white matter with high iron staining intensity in the cortical white matter and low in gray matter (Fig. 8A). The boundaries show a high paramagnetic susceptibility of 0.01 ± 0.006 ppm on QSM (red arrows, Fig. 8A). The cortical gray matter has a susceptibility close to zero (−0.0009 ± 0.002 ppm). One AD patient has moderate beta amyloid staining and relatively weak tau staining in a cortical gray matter region, which shows a diamagnetic susceptibility of −0.003 ± 0.003 ppm (yellow triangle, Fig. 8B). Iron staining clearly highlights the gray-white matter boundaries which match the high paramagnetic susceptibility on QSM (0.003 ± 0.005 ppm; red arrows, Fig. 8B). The other AD patient has a strong staining for beta amyloid, tau and iron (Fig. 8C). The gray-white matter boundaries have a strong paramagnetic susceptibility of 0.008 ± 0.005 ppm (red arrows Fig. 8C). A sub-region within the gray matter has a moderate iron staining but relatively low beta amyloid and tau staining (red circle, Fig. 8C); this sub-region shows a paramagnetic susceptibility of 0.002 ± 0.002 ppm. The sub-region within the gray matter that has high beta amyloid and tau staining (yellow diamond, Fig. 8C), on the other hand, shows a diamagnetic susceptibility of −0.003 ± 0.002 ppm.

4. Discussion

4.1. Magnetic susceptibility of beta amyloid

The present study explicitly showed that beta amyloid has diamagnetic susceptibility property that can be measured by QSM MR imaging (Fig. 1). This finding is consistent with the fact that amino acids generally have diamagnetic susceptibility. The amino acid sequence of human beta amyloid 1–42 is: H - Asp - Ala - Glu - Phe - Gly - His - Asp - Ser - Gly - Phe - Glu - Val - Arg - His - Gln - Lys - Leu - Val - Phe - Phe - Ala - Glu - Asp - Val - Gly - Ser - Asn - Lys - Gly - Ala - Ile - Ile - Gly - Leu - Met - Val - Gly - Gly - Val - Val - Ile - Ala – OH (Link, 1995). Aspartic acid (Asp), Alanine (Ala), Glutamic acid (Glu), Glycine (Gly), and Valine (Val) have molar magnetic susceptibility values (in CGS) of -64.2×10^{-6} cm^3/mol, -50.5×10^{-6} cm^3/mol, -78.5×10^{-6} cm^3/mol, -40.3×10^{-6} cm^3/mol, and $-74.3 \times 10^{-6\,\mathrm{cm3}}$/mol respectively (Hodgman, 1951). Susceptibility values of those amino acids without documented molar susceptibility, e.g. Methionine (Met), can be estimated by taking other amino acid as reference, e.g., if Aspartic acid was taken as reference: Susceptibility (Methionine) = Susceptibility (Aspartic acid) × Molar mass ratio (Methionine/Aspartic acid). An averaged value in reference to all other known amino acids can be used to reduce bias. The magnetic susceptibility of a single beta amyloid 1–42 peptide can be estimated as the sum of the susceptibility values of its component amino acids, which is at around $-3126.4 \times 10^{-6\,\mathrm{cm3}}$/mol. A similar first order estimation of molar mass of beta amyloid 1–42 peptide was 5191.1 g/mol. Although parts of amyloid fibril have coherent conformations of β-sheet and α-helix (Luhrs et al., 2005; Serpell, 2000), amyloid plaques are mostly clumps of disordered beta amyloid peptides. The reported twofold beta-sheet amyloid fibrils have a mass density about 1.7 g/cm^3 (Xu and Buehler, 2010). Following the conversion from molar susceptibility to volume susceptibility (Liu et al., 2015a), the estimated lower bound of volume susceptibility of pure beta amyloid fibrils is around −12.86 ppm and its susceptibility value relative to water (−9.03 ppm) is −3.83 ppm.

The susceptibility difference between assay buffer and beta amyloid with buffer is around -5×10^{-3} ppm, which can be attributed solely to the diamagnetism of beta amyloid. The measured susceptibility

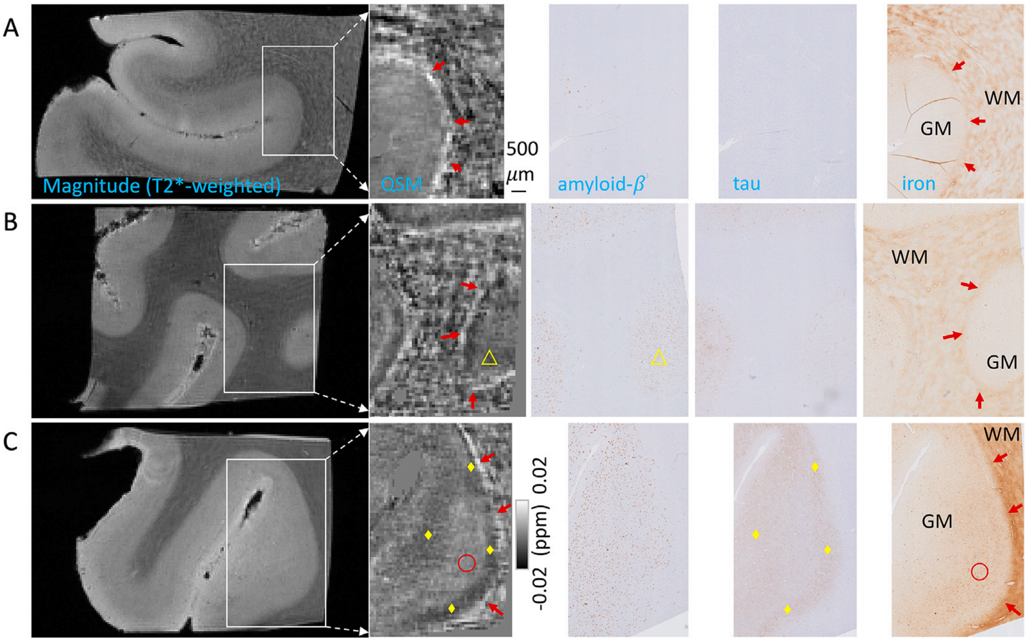

Fig. 8. Comparison of QSM and histological stainings of amyloid-β, tau and iron in the frontal cortex of a control (A) and two AD patients (B&C). (A) Control: QSM shows hyper intense paramagnetic susceptibility at gray-white matter boundaries that matches the iron staining (red arrows). Cortical gray matter shows low staining for amyloid-β, tau and iron and has a susceptibility near zero. (B) AD patient #1: QSM shows hyper intense paramagnetic susceptibility at the gray-white matter boundaries that matches the iron staining (red arrows). One cortical gray matter region shows moderate amyloid-β staining (yellow triangle) and low tau staining, which has diamagnetic susceptibility. (C) AD patient #2: Hyper intense paramagnetic susceptibility at the gray-white matter boundaries matches iron staining (red arrows). One sub-region in the gray matter has moderate iron staining but low amyloid-β and tau staining (red circle), which shows paramagnetic susceptibility. Another sub-region in the gray matter has strong amyloid-β and tau staining (yellow diamond), which shows diamagnetic susceptibility.

(absolute) value of beta amyloid in our phantom (around −0.005 ppm) and those of suspected amyloid plaques on *ex vivo* QSM maps (around −0.03 ppm) were smaller than the theoretically estimated susceptibility value (−3.83 ppm). Assuming the estimated volume susceptibility of beta amyloid fibrils is accurate, linear fitting of the measured susceptibility would give beta-sheet amyloid fibrils concentrations of 2.22 mg/ml in the phantom and 13.21 mg/cm^3 in *ex vivo* specimens. Beta amyloid peptide used in the phantom was not pure twofold beta-sheet amyloid fibrils, which could explain the higher estimated concentration of 2.22 mg/ml as compared to 0.25 mg/ml used in our experiment. On the other hand, a reverse estimation based on the measured -5×10^{-3} ppm in the phantom would give an estimated mass density of 1.2 g/cm^3, which is reasonably smaller than 1.7 g/cm^3 due to its formation of native aggregates rather than strictly stacked beta-sheet fibrils. A native formation may result in susceptibility cancelation due to possible anisotropic effect of peptide susceptibility.

Adding tau proteins to the buffer produced increased diamagnetism, demonstrating that tau proteins are significantly diamagnetic. Quantitative measurements of the indirect effects of tau protein using diffusion, chemical exchange saturation transfer or perfusion methods have previously reported group differences between wild type mice and transgenic mice that exhibited abnormal tau protein deposition (Holmes et al., 2016; Wells et al., 2015). Our data suggested that tau aggregation could be also directly imaged and quantified based on its magnetic susceptibility using MRI, given sufficient concentration and image resolution. Notice that the susceptibility of tau solution and buffer had a trend of decreasing with increasing TE. This can be attributed to compartmentalization effect of molecules within the imaging voxels (Cronin et al., 2017), although figuring out the exact molecular components of the tau protein solutions is beyond the scope of this study.

4.2. *In vivo age-correlated change of susceptibility*

Studies have evaluated the capability of QSM for detecting white matter demyelination and iron deposition in normal aging (Gong et al., 2015; Li et al., 2014), Parkinson's disease (He et al., 2016; Langkammer et al., 2016; Li et al., 2016), subjects with AD (Acosta-Cabronero et al., 2013; Ayton et al., 2017; Moon et al., 2016), and a mouse model of tauopathy (O'Callaghan et al., 2017). So far consensus has been reached that iron and myelin contents are two prime contributors to paramagnetism and diamagnetism in brain tissues (Liu et al., 2015b). Both age-related increases and decreases were observed in *in vivo* Aβ mouse brains.

The voxel-wise longitudinal analysis revealed widespread negative correlations between susceptibility value and age in Aβ mice, with large clusters located in gray matter regions including the forebrain cortex, midbrain, cerebellar cortex and thalamus (Fig. 2), where abnormal beta amyloid depositions are expected in this transgenic model (Davis et al., 2004), as well as in white matter fiber tracts including the corpus callosum, fornix and anterior commissure. The observed age-related increase in diamagnetism surrounding white matter tracts including the corpus callosum, fornix and anterior commissure is consistent with the aggregation of beta amyloid plaques in nearby regions, as noticeable in thioflavin-S stain for beta amyloid. Supporting this hypothesis, a previous study of human AD patients that used diffusion MRI and PET imaging showed possible beta amyloid aggregation in areas near white matter tracts including the corpus callosum, hippocampal cingulum, and lateral fornix (Racine et al., 2014). Similarly, beta amyloid accumulation in white matter independent of overall gray matter fibrillar amyloid pathology has also been reported in AD patients (Collins-Praino et al., 2014). The increase in diamagnetism surrounding white matter might also be induced by myelination (Lee et al., 2012; Liu et al., 2011b), although myelin content is not expected to increase with aging in late adulthood. The absence of similar negative correlations in the control group ruled out this possibility. A previous study of myelination processes in mouse corpus callosum has reported that the highest rate of myelination happens before the age of 45 days. The rate decreased greatly afterwards, exhibiting nearly a flat projection along age after 45 days (Sturrock, 1980). This explains why a possible myelination process in major white matter tracts was not captured by the linear regression analysis between susceptibility and age (from 70 days to 538 days) in our study.

In our beta amyloid mice, significant positive correlations of susceptibility with age were observed in the caudate putamen, hypothalamus, substantia innominata, as well as somatosensory areas of the cerebral cortex. In contrast, no significant positive correlation with age was observed in the control group, suggesting that the change in susceptibility in these regions is due to Aβ-associated pathological changes. In the left hippocampus where the earliest deposition of beta amyloid 40 and 42 peptides was reported (Davis et al., 2004), significantly higher susceptibility value was observed in Aβ mice as compared to the control group at the age of 216 days. The higher susceptibility is consistent with previous reports of iron deposition accompanying aggregation of beta amyloid. For instance, an increase in labile iron (Fe^{2+}) associated with AD pathology has been well recognized by previous studies (Goodman, 1953; Smith et al., 1997). It is believed that iron can be stored within amyloid aggregates (Everett et al., 2014) and promote toxicity of beta amyloid peptide (Liu et al., 2011a). A recent study found that ferric (Fe3+), ferrous (Fe2+) iron and magnetite all exist in amyloid plagues (Telling et al., 2017). On *ex vivo* QSM maps relatively high QSM values were observed in the hippocampus as in caudate putamen. However, in Prussian blue stain, the concentration of stained iron in the hippocampus was not as high as in the caudate putamen, suggesting existence of iron in other states such as ferrous iron and those stored in ferritin that possess a protein surface which is difficult to infiltrate (Meadowcroft et al., 2009). Possible increase in ferritin content in activated microglia and astrogliosis in the hippocampus may indicate inflammation around senile plaques (Zeineh et al., 2015).

4.3. *Validation with high resolution ex vivo images and histology*

High-resolution *ex vivo* images of the post-mortem Aβ mouse revealed individual amyloid plaques that exhibited strong diamagnetism in the hippocampus, somatosensory cortex, entorhinal cortex and dorsal auditory cortex (Fig. 3), where abnormal beta amyloid aggregation is known to occur in this transgenic mouse model (Davis et al., 2004). One of the most striking findings lies in the comparison between *in vivo* longitudinal analysis and post-mortem *ex vivo* images. The clusters exhibiting significant negative correlations on *in vivo* images had a nearly perfect spatial correspondence with focal regions of evident negative susceptibility values on *ex vivo* high-resolution susceptibility maps (Fig. 4). Although ProHance could induce a general increase of susceptibility value on *ex vivo* images, this spatial correspondence indicated that magnetic susceptibility could be further explored as an effective non-invasive imaging biomarker for not only detecting the presence of beta amyloid plaque, but also monitoring its aggregation longitudinally.

Histological staining further confirmed that quantitative susceptibility maps were able to reflect underlying macromolecular abnormalities in AD (Figs. 6 and 7). While the limitations of histology including, specifically the destructive, 2D and non-quantitative nature of histological staining, have prevented a quantitative comparison, quantitative susceptibility maps qualitatively agreed with histology. Prussian blue is sensitive to ferric iron but not ferrous iron. Further, iron stored within ferritin or packed within plaques may not have sufficient Prussian blue reaction due to the difficulty for stain to infiltrate into the protein and plaque surface (Meadowcroft et al., 2009). Therefore, high concentration of ferritin contained in densely packed neurons in the spyramidal layer and stratum oriens of the hippocampus may not exhibit strong staining, though they can still manifest high intensity on paramagnetic susceptibility map, unrestricted by the feasibility of molecular reaction.

4.4. Implications for AD imaging and limitations

Beta amyloid peptides are crucially involved in AD as the main component of plaques. Currently the only well-established method for identifying individual amyloid plaque is post-mortem histological analysis. Plaques are very small with an average size of 20 μm (Serrano-Pozo et al., 2012; Yan et al., 2009) and generally require high-resolution scan for visualization. Iron is also critically involved in AD. The ability to map both beta amyloid and iron at high spatial resolution may provide a means to track their evolution over time simultaneously, thus enabling studies of disease progression and prediction (Fig. 8). A recent QSM study of human AD patients reported that a higher iron load was correlated with greater cognitive decline and, combined with amyloid PET scans, QSM might provide higher predictive value (Ayton et al., 2017).

However, in addition to beta amyloid, tau protein and myelin are also diamagnetic. Co-localization of iron and beta amyloid could generate counteracting effects on QSM maps (Fig. 8), and reduce the contrast from amyloid plaques especially in human bran when large iron load often exists around amyloid plaques. In addition, clinical MRI can hardly achieve the ultra-high resolution used in this study on tissue sample and mouse models. These may reduce the specificity of diamagnetic susceptibility map in serving as a macromolecular quantification tool in clinical settings. Our study found that diamagnetic susceptibility map and paramagnetic susceptibility map bear high sensitivity in capturing pathology-related abnormalities in Alzheimer's disease. These findings call for further development of a technique to generate separate markers based on magnetic susceptibility for aggregated proteins and associated iron.

5. Conclusion

We demonstrated in a phantom that beta amyloid was diamagnetic and can generate strong contrast on susceptibility maps. Based on this, it is further shown both *in vivo* and *ex vivo* that magnetic susceptibility mapping could be used to detect accumulation of amyloid plaques in AD mouse models. Most notably, the diamagnetic susceptibility map and paramagnetic susceptibility map provided image contrast for identifying dominating magnetic sources of beta amyloid plaques or iron, which were further validated by histology.

Appendix A. Supplementary data

Supplementary data to this article can be found online at https://doi.org/10.1016/j.neuroimage.2019.02.019.

References

Acosta-Cabronero, J., Williams, G.B., Cardenas-Blanco, A., Arnold, R.J., Lupson, V., Nestor, P.J., 2013. In vivo quantitative susceptibility mapping (QSM) in Alzheimer's disease. PLoS One 8, e81093.

Albert, M.S., DeKosky, S.T., Dickson, D., Dubois, B., Feldman, H.H., Fox, N.C., Gamst, A., Holtzman, D.M., Jagust, W.J., Petersen, R.C., Snyder, P.J., Carrillo, M.C., Thies, B., Phelps, C.H., 2011. The diagnosis of mild cognitive impairment due to Alzheimer's disease: recommendations from the National Institute on Aging-Alzheimer's Association workgroups on diagnostic guidelines for Alzheimer's disease. Alzheimers Dement 7, 270–279.

Ayton, S., Fazlollahi, A., Bourgeat, P., Raniga, P., Ng, A., Lim, Y.Y., Diouf, I., Farquharson, S., Fripp, J., Ames, D., Doecke, J., Desmond, P., Ordidge, R., Masters, C.L., Rowe, C.C., Maruff, P., Villemagne, V.L., , Australian Imaging, B., Lifestyle Research, G., Salvado, O., Bush, A.I., 2017. Cerebral quantitative susceptibility mapping predicts amyloid-beta-related cognitive decline. Brain 140, 2112–2119.

Babaei, M., Jones, I.C., Dayal, K., Mauter, M.S., 2017. Computing the diamagnetic susceptibility and diamagnetic anisotropy of membrane proteins from structural subunits. J. Chem. Theor. Comput. 13, 2945–2953.

Benilova, I., Karran, E., De Strooper, B., 2012. The toxic Abeta oligomer and Alzheimer's disease: an emperor in need of clothes. Nat. Neurosci. 15, 349–357.

Borthakur, A., Gur, T., Wheaton, A.J., Corbo, M., Trojanowski, J.Q., Lee, V.M., Reddy, R., 2006. In vivo measurement of plaque burden in a mouse model of Alzheimer's disease. J. Magn. Reson. Imag. 24, 1011–1017.

Bulk, M., Abdelmoula, W.M., Nabuurs, R.J.A., van der Graaf, L.M., Mulders, C.W.H., Mulder, A.A., Jost, C.R., Koster, A.J., van Buchem, M.A., Natte, R., Dijkstra, J., van der Weerd, L., 2018. Postmortem MRI and histology demonstrate differential iron accumulation and cortical myelin organization in early- and late-onset Alzheimer's disease. Neurobiol. Aging 62, 231–242.

Chamberlain, R., Reyes, D., Curran, G.L., Marjanska, M., Wengenack, T.M., Poduslo, J.F., Garwood, M., Jack Jr., C.R., 2009. Comparison of amyloid plaque contrast generated by T2-weighted, T2*-weighted, and susceptibility-weighted imaging methods in transgenic mouse models of Alzheimer's disease. Magn. Reson. Med. 61, 1158–1164.

Collins-Praino, L.E., Francis, Y.I., Griffith, E.Y., Wiegman, A.F., Urbach, J., Lawton, A., Honig, L.S., Cortes, E., Vonsattel, J.P., Canoll, P.D., Goldman, J.E., Brickman, A.M., 2014. Soluble amyloid beta levels are elevated in the white matter of Alzheimer's patients, independent of cortical plaque severity. Acta Neuropathol. Commun. 2, 83.

Cook, C., Dunmore, J.H., Murray, M.E., Scheffel, K., Shukoor, N., Tong, J., Castanedes-Casey M, Phillips, V., Rousseau, L., Penuliar, M.S., Kurti, A., Dickson, D.W., Petrucelli, L., Fryer, J.D., 2014. Severe amygdala dysfunction in a MAPT transgenic mouse model of frontotemporal dementia. Neurobiol. Aging 35, 1769–1777.

Cronin, M.J., Wang, N., Decker, K.S., Wei, H., Zhu, W.Z., Liu, C., 2017. Exploring the origins of echo-time-dependent quantitative susceptibility mapping (QSM) measurements in healthy tissue and cerebral microbleeds. Neuroimage 149, 98–113.

Davis, J., Xu, F., Deane, R., Romanov, G., Previti, M.L., Zeigler, K., Zlokovic, B.V., Van Nostrand, W.E., 2004. Early-onset and robust cerebral microvascular accumulation of amyloid beta-protein in transgenic mice expressing low levels of a vasculotropic Dutch/Iowa mutant form of amyloid beta-protein precursor. J. Biol. Chem. 279, 20296–20306.

Deistung, A., Schweser, F., Reichenbach, J.R., 2017. Overview of quantitative susceptibility mapping. NMR Biomed. 30.

Dhenain, M., Privat, N., Duyckaerts, C., Jacobs, R.E., 2002a. Senile plaques do not induce susceptibility effects in T2*-weighted MR microscopic images. NMR Biomed. 15, 197–203.

Dhenain, M., Privat, N., Duyckaerts, C., Jacobs, R.E., 2002b. Senile plaques do not induce susceptibility effects in T-2*-weighted MR microscopic images. NMR Biomed. 15, 197–203.

Dubois, B., Feldman, H.H., Jacova, C., Hampel, H., Molinuevo, J.L., Blennow, K., DeKosky, S.T., Gauthier, S., Selkoe, D., Bateman, R., Cappa, S., Crutch, S., Engelborghs, S., Frisoni, G.B., Fox, N.C., Galasko, D., Habert, M.O., Jicha, G.A., Nordberg, A., Pasquier, F., Rabinovici, G., Robert, P., Rowe, C., Salloway, S., Sarazin, M., Epelbaum, S., de Souza, L.C., Vellas, B., Visser, P.J., Schneider, L., Stern, Y., Scheltens, P., Cummings, J.L., 2014. Advancing research diagnostic criteria for Alzheimer's disease: the IWG-2 criteria. Lancet Neurol. 13, 614–629.

El Tannir El Tayara, N., Delatour, B., Le Cudennec, C., Guegan, M., Volk, A., Dhenain, M., 2006. Age-related evolution of amyloid burden, iron load, and MR relaxation times in a transgenic mouse model of Alzheimer's disease. Neurobiol. Dis. 22, 199–208.

El Tayara Nel, T., Volk, A., Dhenain, M., Delatour, B., 2007. Transverse relaxation time reflects brain amyloidosis in young APP/PS1 transgenic mice. Magn. Reson. Med. 58, 179–184.

Everett, J., Cespedes, E., Shelford, L.R., Exley, C., Collingwood, J.F., Dobson, J., van der Laan, G., Jenkins, C.A., Arenholz, E., Telling, N.D., 2014. Ferrous iron formation following the co-aggregation of ferric iron and the Alzheimer's disease peptide beta-amyloid (1-42). J. R. Soc. Interface 11, 20140165.

Falangola, M.F., Lee, S.P., Nixon, R.A., Duff, K., Helpern, J.A., 2005. Histological co-localization of iron in A beta plaques of PS/APP transgenic mice. Neurochem. Res. 30, 201–205.

Gong, N.J., Chan, C.C., Leung, L.M., Wong, C.S., Dibb, R., Liu, C., 2017 May. Differential microstructural and morphological abnormalities in mild cognitive impairment and Alzheimer's disease: evidence from cortical and deep gray matter. Hum. Brain Mapp. 38 (5), 2495–2508. https://doi.org/10.1002/hbm.23535. Epub 2017 Feb 8.

Gong, N.J., Kuzminski, S., Clark, M., Fraser, M., Sundman, M., Guskiewicz, K., Petrella, J.R., Liu, C., 2018. Microstructural alterations of cortical and deep gray matter over a season of high school football revealed by diffusion kurtosis imaging. Neurobiol. Dis. 119, 79–87.

Gong, N.J., Wong, C.S., Chan, C.C., Leung, L.M., Chu, Y.C., 2013. Correlations between microstructural alterations and severity of cognitive deficiency in Alzheimer's disease and mild cognitive impairment: a diffusional kurtosis imaging study. Magn. Reson. Imaging 31, 688–694.

Gong, N.J., Wong, C.S., Hui, E.S., Chan, C.C., Leung, L.M., 2015. Hemisphere, gender and age-related effects on iron deposition in deep gray matter revealed by quantitative susceptibility mapping. NMR Biomed. 28, 1267–1274.

Goodman, L., 1953. Alzheimer's disease; a clinico-pathologic analysis of twenty-three cases with a theory on pathogenesis. J. Nerv. Ment. Dis. 118, 97–130.

Haacke, E.M., Liu, S., Buch, S., Zheng, W., Wu, D., Ye, Y., 2015. Quantitative susceptibility mapping: current status and future directions. Magn. Reson. Imaging 33, 1–25.

Hardy, J.A., Higgins, G.A., 1992. Alzheimer's disease: the amyloid cascade hypothesis. Science 256, 184–185.

He, N., Huang, P., Ling, H., Langley, J., Liu, C., Ding, B., Huang, J., Xu, H., Zhang, Y., Zhang, Z., Hu, X., Chen, S., Yan, F., 2016. Dentate nucleus iron deposition is a potential biomarker for tremor-dominant Parkinson's disease. NMR Biomed.

Helpern, J.A., Lee, S.P., Falangola, M.F., Dyakin, V.V., Bogart, A., Ardekani, B., Duff, K., Branch, C., Wisniewski, T., de Leon, M.J., Wolf, O., O'Shea, J., Nixon, R.A., 2004. MRI assessment of neuropathology in a transgenic mouse model of Alzheimer's disease. Magn. Reson. Med. 51, 794–798.

Hodgman, C.D., 1951. Handbook of Chemistry and Physics. LWW.

Holmes, H.E., Colgan, N., Ismail, O., Ma, D., Powell, N.M., O'Callaghan, J.M., Harrison, I.F., Johnson, R.A., Murray, T.K., Ahmed, Z., Heggenes, M., Fisher, A., Cardoso, M.J., Modat, M., Walker-Samuel, S., Fisher, E.M.C., Ourselin, S., O'Neill, M.J., Wells, J.A., Collins, E.C., Lythgoe, M.F., 2016. Imaging the accumulation and suppression of tau pathology using multiparametric MRI. Neurobiol. Aging 39, 184–194.

Jack, C.R., Garwood, M., Wengenack, T.M., Borowski, B., Curran, G.L., Lin, J., Adriany, G., Grohn, I.H.J., Grimm, R., Poduslo, J.F., 2004. In vivo visualization of Alzheimer's amyloid plaques by magnetic resonance imaging in transgenic mice without a contrast agent. Magn. Reson. Med. 52, 1263–1271.

Jack Jr., C.R., Wengenack, T.M., Reyes, D.A., Garwood, M., Curran, G.L., Borowski, B.J., Lin, J., Preboske, G.M., Holasek, S.S., Adriany, G., Poduslo, J.F., 2005. In vivo magnetic resonance microimaging of individual amyloid plaques in Alzheimer's transgenic mice. J. Neurosci. 25, 10041–10048.

Johnson, G.A., Cofer, G.P., Fubara, B., Gewalt, S.L., Hedlund, L.W., Maronpot, R.R., 2002. Magnetic resonance histology for morphologic phenotyping. J. Magn. Reson. Imag. 16, 423–429.

Klunk, W.E., Engler, H., Nordberg, A., Wang, Y., Blomqvist, G., Holt, D.P., Bergstrom, M., Savitcheva, I., Huang, G.F., Estrada, S., Ausen, B., Debnath, M.L., Barletta, J., Price, J.C., Sandell, J., Lopresti, B.J., Wall, A., Koivisto, P., Antoni, G., Mathis, C.A., Langstrom, B., 2004. Imaging brain amyloid in Alzheimer's disease with Pittsburgh Compound-B. Ann. Neurol. 55, 306–319.

Langkammer, C., Pirpamer, L., Seiler, S., Deistung, A., Schweser, F., Franthal, S., Homayoon, N., Katschnig-Winter, P., Koegl-Wallner, M., Pendl, T., Stoegerer, E.M., Wenzel, K., Fazekas, F., Ropele, S., Reichenbach, J.R., Schmidt, R., Schwingenschuh, P., 2016. Quantitative susceptibility mapping in Parkinson's disease. PLoS One 11, e0162460.

Langkammer, C., Schweser, F., Krebs, N., Deistung, A., Goessler, W., Scheurer, E., Sommer, K., Reishofer, G., Yen, K., Fazekas, F., Ropele, S., Reichenbach, J.R., 2012. Quantitative susceptibility mapping (QSM) as a means to measure brain iron? A post mortem validation study. Neuroimage 62, 1593–1599.

Lee, J., Shmueli, K., Kang, B.T., Yao, B., Fukunaga, M., van Gelderen, P., Palumbo, S., Bosetti, F., Silva, A.C., Duyn, J.H., 2012. The contribution of myelin to magnetic susceptibility-weighted contrasts in high-field MRI of the brain. Neuroimage 59, 3967–3975.

Leskovjan, A.C., Lanzirotti, A., Miller, L.M., 2009. Amyloid plaques in PSAPP mice bind less metal than plaques in human Alzheimer's disease. Neuroimage 47, 1215–1220.

Li, W., Wang, N., Yu, F., Han, H., Cao, W., Romero, R., Tantiwongkosi, B., Duong, T.Q., Liu, C., 2015. A method for estimating and removing streaking artifacts in quantitative susceptibility mapping. Neuroimage 108, 111–122.

Li, W., Wu, B., Batrachenko, A., Bancroft-Wu, V., Morey, R.A., Shashi, V., Langkammer, C., De Bellis, M.D., Ropele, S., Song, A.W., Liu, C., 2014. Differential developmental trajectories of magnetic susceptibility in human brain gray and white matter over the lifespan. Hum. Brain Mapp. 35, 2698–2713.

Li, W., Wu, B., Liu, C., 2011. Quantitative susceptibility mapping of human brain reflects spatial variation in tissue composition. Neuroimage 55, 1645–1656.

Li, X., Harrison, D.M., Liu, H., Jones, C.K., Oh, J., Calabresi, P.A., van Zijl, P.C., 2016. Magnetic susceptibility contrast variations in multiple sclerosis lesions. J. Magn. Reson. Imag. 43, 463–473.

Link, C.D., 1995. Expression of human beta-amyloid peptide in transgenic Caenorhabditis elegans. Proc. Natl. Acad. Sci. U. S. A. 92, 9368–9372.

Lister-James, J., Pontecorvo, M.J., Clark, C., Joshi, A.D., Mintun, M.A., Zhang, W., Lim, N., Zhuang, Z., Golding, G., Choi, S.R., Benedum, T.E., Kennedy, P., Hefti, F., Carpenter, A.P., Kung, H.F., Skovronsky, D.M., 2011. Florbetapir f-18: a histopathologically validated Beta-amyloid positron emission tomography imaging agent. Semin. Nucl. Med. 41, 300–304.

Liu, B., Moloney, A., Meehan, S., Morris, K., Thomas, S.E., Serpell, L.C., Hider, R., Marciniak, S.J., Lomas, D.A., Crowther, D.C., 2011a. Iron promotes the toxicity of amyloid beta peptide by impeding its ordered aggregation. J. Biol. Chem. 286, 4248–4256.

Liu, C., Li, W., Johnson, G.A., Wu, B., 2011b. High-field (9.4 T) MRI of brain dysmyelination by quantitative mapping of magnetic susceptibility. Neuroimage 56, 930–938.

Liu, C., Li, W., Tong, K.A., Yeom, K.W., Kuzminski, S., 2015a. Susceptibility-weighted imaging and quantitative susceptibility mapping in the brain. J. Magn. Reson. Imag. 42, 23–41.

Liu, C., Wei, H., Gong, N.J., Cronin, M., Dibb, R., Decker, K., 2015b. Quantitative susceptibility mapping: contrast mechanisms and clinical applications. Tomography 1, 3–17.

Luhrs, T., Ritter, C., Adrian, M., Riek-Loher, D., Bohrmann, B., Dobeli, H., Schubert, D., Riek, R., 2005. 3D structure of Alzheimer's amyloid-beta(1-42) fibrils. Proc. Natl. Acad. Sci. U. S. A. 102, 17342–17347.

Meadowcroft, M.D., Connor, J.R., Smith, M.B., Yang, Q.X., 2009. MRI and histological analysis of beta-amyloid plaques in both human Alzheimer's disease and APP/PS1 transgenic mice. J. Magn. Reson. Imag. 29, 997–1007.

Meadowcroft, M.D., Peters, D.G., Dewal, R.P., Connor, J.R., Yang, Q.X., 2015. The effect of iron in MRI and transverse relaxation of amyloid-beta plaques in Alzheimer's disease. NMR Biomed. 28, 297–305.

Moon, Y., Han, S.H., Moon, W.J., 2016. Patterns of brain iron accumulation in vascular dementia and Alzheimer's dementia using quantitative susceptibility mapping imaging. J. Alzheim. Dis. 51, 737–745.

O'Callaghan, J., Holmes, H., Powell, N., Wells, J.A., Ismail, O., Harrison, I.F., Siow, B., Johnson, R., Ahmed, Z., Fisher, A., Meftah, S., O'Neill, M.J., Murray, T.K., Collins, E.C., Shmueli, K., Lythgoe, M.F., 2017. Tissue magnetic susceptibility mapping as a marker of tau pathology in Alzheimer's disease. Neuroimage 159, 334–345.

Poduslo, J.F., Wengenack, T.M., Curran, G.L., Wisniewski, T., Sigurdsson, E.M., Macura, S.I., Borowski, B.J., Jack Jr., C.R., 2002. Molecular targeting of Alzheimer's amyloid plaques for contrast-enhanced magnetic resonance imaging. Neurobiol. Dis. 11, 315–329.

Racine, A.M., Adluru, N., Alexander, A.L., Christian, B.T., Okonkwo, O.C., Oh, J., Cleary, C.A., Birdsill, A., Hillmer, A.T., Murali, D., Barnhart, T.E., Gallagher, C.L., Carlsson, C.M., Rowley, H.A., Dowling, N.M., Asthana, S., Sager, M.A., Bendlin, B.B., Johnson, S.C., 2014. Associations between white matter microstructure and amyloid burden in preclinical Alzheimer's disease: a multimodal imaging investigation. Neuroimage-Clinical 4, 604–614.

Rose, S.E., Janke, A.L., Chalk, J.B., 2008. Gray and white matter changes in Alzheimer's disease: a diffusion tensor imaging study. J. Magn. Reson. Imag. 27, 20–26.

Schweser, F., Deistung, A., Lehr, B.W., Reichenbach, J.R., 2011. Quantitative imaging of intrinsic magnetic tissue properties using MRI signal phase: an approach to in vivo brain iron metabolism? Neuroimage 54, 2789–2807.

Schweser, F., Deistung, A., Reichenbach, J.R., 2016. Foundations of MRI phase imaging and processing for quantitative susceptibility mapping (QSM). Z. Med. Phys. 26, 6–34.

Serpell, L.C., 2000. Alzheimer's amyloid fibrils: structure and assembly. Biochim. Biophys. Acta 1502, 16–30.

Serrano-Pozo, A., Mielke, M.L., Muzitansky, A., Gomez-Isla, T., Growdon, J.H., Bacskai, B.J., Betensky, R.A., Frosch, M.P., Hyman, B.T., 2012. Stable size distribution of amyloid plaques over the course of Alzheimer disease. J. Neuropathol. Exp. Neurol. 71, 694–701.

Sisodia, S.S., Price, D.L., 1995. Role of the beta-amyloid protein in Alzheimer's disease. FASEB J. 9, 366–370.

Smith, M.A., Harris, P.L.R., Sayre, L.M., Perry, G., 1997. Iron accumulation in Alzheimer disease is a source of redox-generated free radicals. Proc. Natl. Acad. Sci. U. S. A 94, 9866–9868.

Sturrock, R.R., 1980. Myelination of the mouse corpus callosum. Neuropathol. Appl. Neurobiol. 6, 415–420.

Telling, N.D., Everett, J., Collingwood, J.F., Dobson, J., van der Laan, G., Gallagher, J.J., Wang, J., Hitchcock, A.P., 2017. Iron biochemistry is correlated with amyloid plaque morphology in an established mouse model of Alzheimer's disease. Cell Chem Biol 24, 1205–1215 e1203.

van Duijn, S., Nabuurs, R.J., van Duinen, S.G., Natte, R., 2013. Comparison of histological techniques to visualize iron in paraffin-embedded brain tissue of patients with Alzheimer's disease. J. Histochem. Cytochem. 61, 785–792.

Vanhoutte, G., Dewachter, I., Borghgraef, P., Van Leuven, F., Van der Linden, A., 2005. Noninvasive in vivo MRI detection of neuritic plaques associated with iron in APP [V717I] transgenic mice, a model for Alzheimer's disease. Magn. Reson. Med. 53, 607–613.

Wang, Y., Liu, T., 2015. Quantitative susceptibility mapping (QSM): decoding MRI data for a tissue magnetic biomarker. Magn. Reson. Med. 73, 82–101.

Wells, J.A., O'Callaghan, J.M., Holmes, H.E., Powell, N.M., Johnson, R.A., Siow, B., Torrealdea, F., Ismail, O., Walker-Samuel, S., Golay, X., Rega, M., Richardson, S., Modat, M., Cardoso, M.J., Ourselin, S., Schwarz, A.J., Ahmed, Z., Murray, T.K., O'Neill, M.J., Collins, E.C., Colgan, N., Lythgoe, M.F., 2015. In vivo imaging of tau pathology using multi-parametric quantitative MRI. Neuroimage 111, 369–378.

Wengenack, T.M., Reyes, D.A., Curran, G.L., Borowski, B.J., Lin, J., Preboske, G.M., Holasek, S.S., Gilles, E.J., Chamberlain, R., Marjanska, M., Jack, C.R., Garwood, M., Poduslo, J.F., 2011. Regional differences in MRI detection of amyloid plaques in AD transgenic mouse brain. Neuroimage 54, 113–122.

Wu, B., Li, W., Guidon, A., Liu, C., 2012. Whole brain susceptibility mapping using compressed sensing. Magn. Reson. Med. 67, 137–147.

Xu, Z., Buehler, M.J., 2010. Mechanical energy transfer and dissipation in fibrous beta-sheet-rich proteins. Phys. Rev. E - Stat. Nonlinear Soft Matter Phys. 81, 061910.

Yan, P., Bero, A.W., Cirrito, J.R., Xiao, Q., Hu, X., Wang, Y., Gonzales, E., Holtzman, D.M., Lee, J.M., 2009. Characterizing the appearance and growth of amyloid plaques in APP/PS1 mice. J. Neurosci. 29, 10706–10714.

Zeineh, M.M., Chen, Y., Kitzler, H.H., Hammond, R., Vogel, H., Rutt, B.K., 2015. Activated iron-containing microglia in the human hippocampus identified by magnetic resonance imaging in Alzheimer disease. Neurobiol. Aging 36, 2483–2500.